This is the accepted author manuscript. To cite this article, please refer to the published version: Jul Van den Broeck, Emile Vanderstraeten, Pieter Decleer, Dries Vande Ginste. 2023. Conservative second-order accurate finite-difference scheme for the coupled Maxwell-Dirac equations, Applied Mathematical Modelling, 120, 25-39. https://doi.org/10.1016/j.apm.2023.03.016

Conservative Second-Order Accurate Finite-Difference Scheme for the Coupled Maxwell-Dirac Equations

Jul Van den Broeck[a,*], Emile Vanderstraeten[a], Pieter Decleer[a], Dries Vande Ginste[a]

[a] *quest, IDLab, Department of Information Technology, Technologiepark-Zwijnaarde 126, 9000 Gent, Belgium*

Abstract

The recent development of nanoelectronic devices that incorporate Dirac materials has highly increased the need for adequate simulation and modelling tools. This paper introduces an accurate, multiphysics finite-difference time-domain method to solve the pertinent Maxwell-Dirac equations. The stability criterion for the Dirac equation with electromagnetic fields is derived, which reduces to the Courant-Friedrichs-Lewy condition in the absence of electromagnetic fields. Validation examples show the second-order accuracy of the novel fully coupled Maxwell-Dirac scheme and illustrate that total norm and energy are conserved within a relative error of order 10^{-4}. The method is applied to a $ZrTe_5$ waveguide and it is found that even at low field strengths, the charge carriers can be accelerated to 80 % of the Fermi velocity. Furthermore, the flexibility of the advocated method allows for the seamless integration into existing computational electromagnetics frameworks and the possible extension to higher-order schemes.

Keywords: Maxwell-Dirac equations, finite-difference time-domain, multiphysics, numerical solver, conservative methods, numerical stability, $ZrTe_5$ waveguide

1. Introduction

As the downscaling of transistors is reaching the physical limit and Moore's law might be coming to an end, novel research paths are being explored to circumvent the spurious quantum effects that appear at the atomic level [1]. One such path involves the on-chip integration of performance-enhancing materials, such as Dirac materials [2]. In this class of materials electrons are governed by Dirac-like Hamiltonians, allowing for carrier transport at increased velocities compared to conventional semiconductors. This makes them a promising option for the design of faster computational building blocks compared to silicon-on-insulator (SOI) transistors. Examples of Dirac materials include graphene [3], topological insulators [4], and Weyl/Dirac semimetals [5]. Since their recent discovery, three-dimensional (3D) Dirac materials have been integrated into state-of-the-art nanoelectronic devices [6–10], sometimes referred to as "Dirac devices". The extra dimension, compared to two-dimensional (2D) graphene, allows for the construction of more complex structures and enables the inclusion of 3D spin effects [11]. However, the cost-effective design of these novel devices requires modelling techniques that incorporate the electromagnetic (EM), quantum mechanical (QM), and relativistic effects of the high-mobility charge carriers in Dirac materials.

Although numerical methods for solving the time-dependent Dirac equation in three spatial dimensions are prevalent in literature [12–17], only a few schemes for the fully coupled (3+1)D Maxwell-Dirac system have been published [18–22]. To solve the EM part, these methods discretise the well-known wave equations for the EM potentials, while implicitly adopting the Lorenz gauge. Because of this choice, however, the gauge condition is in general not satisfied. Furthermore, since the EM potentials $\boldsymbol{a}$ and ϕ are solved for in these works, the implementation of well-established and state-of-the-art numerical techniques, known from computational electromagnetism (CEM) (e.g. [23–26]), of perfectly matched layers (PMLs) [23], and of dielectric materials [27] becomes extremely tedious, as these require the computation of the EM fields $\boldsymbol{e}$ and $\boldsymbol{h}$ rather than the EM potentials. Moreover, the spatial discretisation of the Dirac spinor in [18–22] is performed on a regular grid. This inevitably leads to the fermion doubling problem [28, 29]. Hence, there is still a need for improved schemes that alleviate these shortcomings, and that are easily integrated with existing CEM methods.

*Corresponding author

Email addresses: Jul.VandenBroeck@UGent.be (Jul Van den Broeck), Emile.Vanderstraeten@UGent.be (Emile Vanderstraeten), Pieter.Decleer@UGent.be (Pieter Decleer), Dries.VandeGinste@UGent.be (Dries Vande Ginste)

Therefore, we propose a novel scheme to self-consistently solve the coupled (3+1)D Maxwell-Dirac equations. It improves upon the scheme presented in [16] for the Dirac equation, which reduces the fermion doubling problem, and combines it with the finite-difference time-domain (FDTD) method [23] for Maxwell's curl equations, making it compatible with existing EM solvers. The EM and QM parts are coupled by introducing minimal coupling. We calculate the EM potentials in the Lorenz gauge, which is hence exactly satisfied, and also propose a new discretisation of the quantum current density. Furthermore, meaningful numerical examples illustrate the second-order accuracy, the conservation properties, the applicability of the advocated technique, and its compatibility with legacy (commercial) EM simulation tools.

In Section 2, the pertinent equations are presented, their discretisation is performed, and the coupling between EM and QM is detailed. The stability of both the individual parts and the proposed fully coupled scheme is discussed. Section 3 presents two examples that validate the scheme in terms of accuracy and correspondence with previous results from literature. Next, in Section 4, a Dirac particle in InAs that is coupled to an EM cavity is simulated, demonstrating the conservative properties of our method. The Dirac equation is then modified to describe charge carriers in the 3D Dirac material $ZrTe_5$ and a model of an EM plane wave incident on a $ZrTe_5$ waveguide is modelled. Finally, the paper is concluded in Section 5 and an outline for further research is provided.

2. FDTD formulation of the Maxwell-Dirac system

2.1. Maxwell's equations

The electric field $\boldsymbol{e}$ and the magnetic field $\boldsymbol{h}$ are governed by Maxwell's equations. The curl equations are discretised according to the FDTD method [23] resulting in

$$\hat{\partial}_t \tilde{\boldsymbol{e}}_{\boldsymbol{m}}^{n+\frac{1}{2}} = \frac{1}{\epsilon_0} \hat{\nabla} \times \hat{\boldsymbol{h}}_{\boldsymbol{m}+\frac{1}{2}}^{n} - \frac{1}{\epsilon_0} \tilde{\boldsymbol{j}}_{\boldsymbol{m}}^{n}, \tag{1a}$$

$$\hat{\partial}_t \hat{\boldsymbol{h}}_{\boldsymbol{m}+\frac{1}{2}}^{n+1} = -\frac{1}{\mu_0} \tilde{\nabla} \times \tilde{\boldsymbol{e}}_{\boldsymbol{m}}^{n+\frac{1}{2}}, \tag{1b}$$

where the discrete calculus notation from [30] was employed. A brief explanation of this notation is provided in Appendix A. In (1), μ_0 and ϵ_0 are the vacuum permeability and permittivity, respectively, and $\tilde{\boldsymbol{j}}$ is the discrete current density. To indicate the spatial location of the discrete vectors, the shorthand $\boldsymbol{m} = (i, j, k)$ and $\boldsymbol{m} + 1/2 = (i + 1/2, j + 1/2, k + 1/2)$ are introduced, where the integers i, j and k denote the indices of the grid points in the three spatial dimensions. The index n corresponds to the time step. The discrete electric field $\tilde{\boldsymbol{e}}$ is therefore a so-called *fore*-vector defined on half-integer time steps, while the discrete magnetic field $\hat{\boldsymbol{h}}$ is a *back*-vector at integer time steps. Fig. 1(a) displays their position on a unit cell, also referred to as the "Yee cell".

It is well-known that this method is stable for time steps Δ_t that obey

$$\mathrm{CN} = c\Delta_t \sqrt{\frac{1}{\Delta_x^2} + \frac{1}{\Delta_y^2} + \frac{1}{\Delta_z^2}} \leq 1, \tag{2}$$

where Δ_l, $l = x, y, z$, are the grid steps in each of the three spatial dimensions. This inequality is commonly referred to as the Courant-Friedrichs-Lewy (CFL) condition [23], with CN the Courant number.

The EM potentials $\boldsymbol{a}$ and ϕ are defined in the conventional way:

$$\boldsymbol{e} = -\nabla\phi - \frac{\partial \boldsymbol{a}}{\partial t}, \tag{3a}$$

$$\boldsymbol{h} = \frac{1}{\mu_0} \boldsymbol{\nabla} \times \boldsymbol{a}, \tag{3b}$$

and the gauge is fixed by enforcing the relativistically invariant Lorenz gauge

$$\boldsymbol{\nabla} \cdot \boldsymbol{a} + \frac{1}{c^2} \frac{\partial \phi}{\partial t} = 0. \tag{4}$$

To retain second-order accuracy, we propose to discretise the magnetic vector potential $\boldsymbol{a}$ as a fore-vector at integer spatial and integer temporal steps, while the discrete electric potential ϕ takes on values at integer spatial grid

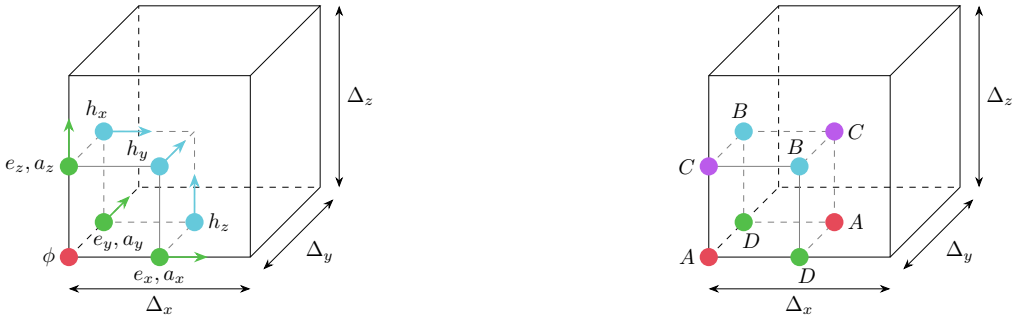

(a) Yee cell

(b) Dirac cell

Figure 1: The spatial grid points on which the discretised (a) EM and (b) Dirac quantities are defined. These unit cells constitute the basic building blocks to construct the entire grid. In (a), the electric quantities $\boldsymbol{e}$ and ϕ are evaluated on half-integer time steps, and the magnetic variables $\boldsymbol{h}$ and $\boldsymbol{a}$ are calculated at integer time steps. In (b), the A and B components are discretised at half-integer time steps, while the C and D components are discretised at integer time steps.

points and half-integer time steps. Their position on the grid is also visualised in Fig. 1(a). This stencil leads to the following discretisation of equation (3a) and (4), respectively:

$$\hat{\partial}_t \tilde{\boldsymbol{a}}_{\boldsymbol{m}}^{n+1} = -\tilde{\nabla}\phi_{\boldsymbol{m}}^{n+\frac{1}{2}} - \tilde{\boldsymbol{e}}_{\boldsymbol{m}}^{n+\frac{1}{2}}, \tag{5a}$$

$$\hat{\partial}_t \phi_{\boldsymbol{m}}^{n+\frac{1}{2}} = -c^2\, \hat{\nabla} \cdot \tilde{\boldsymbol{a}}_{\boldsymbol{m}}^{n}. \tag{5b}$$

Note that these equations can be interpreted as an update scheme for the EM potentials with the electric field acting as a source term.

2.2. Dirac equation

The minimally coupled Dirac equation, in Hartree atomic units, is given by

$$\imath \frac{\partial}{\partial t}\psi = c\,\boldsymbol{\alpha} \cdot (-\imath\nabla - q\boldsymbol{a})\psi + (q\phi + V)\psi + mc^2\beta\psi, \tag{6}$$

where the complex four-component Dirac spinor

$$\psi(\boldsymbol{r}, t) = \begin{pmatrix} A(\boldsymbol{r}, t) \\ B(\boldsymbol{r}, t) \\ C(\boldsymbol{r}, t) \\ D(\boldsymbol{r}, t) \end{pmatrix}$$

is a function of position $\boldsymbol{r}$ and time t. The constants $\imath$, c, m, and q denote the complex unit, the speed of light, the particle mass, and the particle charge, respectively. The external potential V is only a function of the position in this paper. The 4×4 α- and β-matrices are defined as follows:

$$\begin{aligned} \boldsymbol{\alpha} &= \alpha_x \boldsymbol{u}_x + \alpha_y \boldsymbol{u}_y + \alpha_z \boldsymbol{u}_z, \\ \alpha_l &= \begin{pmatrix} 0 & \sigma_l \\ \sigma_l & 0 \end{pmatrix}, \qquad && l = x, y, z, \\ \beta &= \begin{pmatrix} \mathbb{1}_2 & 0 \\ 0 & -\mathbb{1}_2 \end{pmatrix}, \end{aligned}$$

with $\boldsymbol{u}_l$, $l = x, y, z$, the unit basis vectors, $\mathbb{1}_n$ the $n\times n$ identity matrix, and σ_l the Pauli matrices,

$$\sigma_x = \begin{pmatrix} 0 & 1 \\ 1 & 0 \end{pmatrix}, \qquad \sigma_y = \begin{pmatrix} 0 & -\imath \\ \imath & 0 \end{pmatrix}, \qquad \sigma_z = \begin{pmatrix} 1 & 0 \\ 0 & -1 \end{pmatrix}.$$

2.2.1. Discretisation

As a starting point, the discretisation of the Dirac spinor is performed in accordance with the numerical scheme presented in [16]. The corresponding stencil is summarised as follows:

$$\begin{aligned}
A(\boldsymbol{r},t) \quad &\text{on} \quad A^{n-\frac{1}{2}}_{i,j,k} \qquad\quad \text{and} \quad A^{n-\frac{1}{2}}_{i+\frac{1}{2},j+\frac{1}{2},k},\\
B(\boldsymbol{r},t) \quad &\text{on} \quad B^{n-\frac{1}{2}}_{i+\frac{1}{2},j,k+\frac{1}{2}} \quad \text{and} \quad B^{n-\frac{1}{2}}_{i,j+\frac{1}{2},k+\frac{1}{2}},\\
C(\boldsymbol{r},t) \quad &\text{on} \quad C^{n}_{i,j,k+\frac{1}{2}} \qquad\quad \text{and} \quad C^{n}_{i+\frac{1}{2},j+\frac{1}{2},k+\frac{1}{2}},\\
D(\boldsymbol{r},t) \quad &\text{on} \quad D^{n}_{i+\frac{1}{2},j,k} \qquad\quad \text{and} \quad D^{n}_{i,j+\frac{1}{2},k}.
\end{aligned}$$

A visual representation of this discretisation is depicted in Fig. 1(b). The components of the spinor are defined on a space-time grid in a staggered way, such that the resulting discrete Dirac equation is second-order accurate in space and time. Furthermore, as predicted by fermion lattice theory [28, 29], the staggering decreases the amount of unknowns to solve for, leading to a higher computational efficiency, and reduces the amount of fermion doubling.

This scheme was constructed to solve the Dirac equation by itself, but the coupling with Maxwell's equations is required for the complete modelling of nanoelectronic devices. In [16], the vector potential is already introduced in the scheme by applying the Peierls substitution [31]. However, this approach entails an approximation and also requires the calculation of computationally intensive line integrals. This section proposes an alternative and generally valid method that makes use of minimal coupling [32] in an efficient way, leading to a new update scheme for the Dirac equation under the influence of an EM field. The coupling introduces the extra terms $-qc\boldsymbol{\alpha}\cdot\boldsymbol{a}\psi$ and $q\phi\psi$ in (6), which are discretised as follows: First, the discretised EM potentials $\tilde{\boldsymbol{a}}$ and ϕ from (5) are interpolated to the correct grid points in (3+1)D spacetime. Then, for the magnetic vector potential term, the spinor components are interpolated along the corresponding component of the vector potential $\boldsymbol{a}$. This method ensures second-order accuracy as only central differences are used. The result is the following coupled system of discrete update equations:

$$\begin{aligned}
\hat{\partial}_t A^{n+\frac{1}{2}}_{i,j,k} = -\imath c\Big[\hat{\mathcal{D}}_x|^n_{i,j,k} D^n_{i+\frac{1}{2},j,k} - \imath\hat{\mathcal{D}}_y|^n_{i,j,k} D^n_{i,j+\frac{1}{2},k} + \hat{\mathcal{D}}_z|^n_{i,j,k} C^n_{i,j,k+\frac{1}{2}}\Big]\\
- \imath\Big(mc^2 + q\phi^n_{i,j,k} + V^n_{i,j,k}\Big)\tilde{\mathcal{M}}_t A^{n-\frac{1}{2}}_{i,j,k},
\end{aligned} \tag{7a}$$

$$\begin{aligned}
\hat{\partial}_t B^{n+\frac{1}{2}}_{i+\frac{1}{2},j,k+\frac{1}{2}} = -\imath c\Big[\hat{\mathcal{D}}_x|^n_{i+\frac{1}{2},j,k+\frac{1}{2}} C^n_{i+1,j,k+\frac{1}{2}} + \imath\hat{\mathcal{D}}_y|^n_{i+\frac{1}{2},j,k+\frac{1}{2}} C^n_{i+\frac{1}{2},j+\frac{1}{2},k+\frac{1}{2}} - \hat{\mathcal{D}}_z|^n_{i+\frac{1}{2},j,k+\frac{1}{2}} D^n_{i+\frac{1}{2},j,k+1}\Big]\\
- \imath\Big(mc^2 + q\phi^n_{i+\frac{1}{2},j,k+\frac{1}{2}} + V^n_{i+\frac{1}{2},j,k+\frac{1}{2}}\Big)\tilde{\mathcal{M}}_t B^{n-\frac{1}{2}}_{i+\frac{1}{2},j,k+\frac{1}{2}},
\end{aligned} \tag{7b}$$

$$\begin{aligned}
\hat{\partial}_t C^{n+1}_{i,j,k+\frac{1}{2}} = -\imath c\Big[\hat{\mathcal{D}}_x|^{n+\frac{1}{2}}_{i,j,k+\frac{1}{2}} B^{n+\frac{1}{2}}_{i+\frac{1}{2},j,k+\frac{1}{2}} - \imath\hat{\mathcal{D}}_y|^{n+\frac{1}{2}}_{i,j,k+\frac{1}{2}} B^{n+\frac{1}{2}}_{i,j+\frac{1}{2},k+\frac{1}{2}} + \hat{\mathcal{D}}_z|^{n+\frac{1}{2}}_{i,j,k+\frac{1}{2}} A^{n+\frac{1}{2}}_{i,j,k+1}\Big]\\
- \imath\Big(-mc^2 + q\phi^{n+\frac{1}{2}}_{i,j,k+\frac{1}{2}} + V^{n+\frac{1}{2}}_{i,j,k+\frac{1}{2}}\Big)\tilde{\mathcal{M}}_t C^n_{i,j,k+\frac{1}{2}},
\end{aligned} \tag{7c}$$

$$\begin{aligned}
\hat{\partial}_t D^{n+1}_{i+\frac{1}{2},j,k} = -\imath c\Big[\hat{\mathcal{D}}_x|^{n+\frac{1}{2}}_{i+\frac{1}{2},j,k} A^{n+\frac{1}{2}}_{i+1,j,k} + \imath\hat{\mathcal{D}}_y|^{n+\frac{1}{2}}_{i+\frac{1}{2},j,k} A^{n+\frac{1}{2}}_{i+\frac{1}{2},j+\frac{1}{2},k} - \hat{\mathcal{D}}_z|^{n+\frac{1}{2}}_{i+\frac{1}{2},j,k} B^{n+\frac{1}{2}}_{i+\frac{1}{2},j,k+\frac{1}{2}}\Big]\\
- \imath\Big(-mc^2 + q\phi^{n+\frac{1}{2}}_{i+\frac{1}{2},j,k} + V^{n+\frac{1}{2}}_{i+\frac{1}{2},j,k}\Big)\tilde{\mathcal{M}}_t D^n_{i+\frac{1}{2},j,k},
\end{aligned} \tag{7d}$$

where the discrete analogue of the gauge covariant derivative $\mathcal{D}$ is defined as

$$\mathcal{D}_l|^n_{i,j,k} = \partial_l - \imath q a_l|^n_{i,j,k}\mathcal{M}_l, \qquad \text{for } l = x, y, z,$$

and $\mathcal{M}_\mu$, $\mu = t, x, y, z$, represents the averaging operator in each of the four space-time directions. Again, a hat and a tilde indicate backward and forward operators, respectively. The remaining discrete components are determined analogously. The Dirac spinor is then updated by leveraging these eight equations in a leapfrog manner, i.e., first, A and B are advanced to time step $n + 1/2$, next, C and D to $n + 1$.

2.2.2. Stability

A von Neumann stability analysis is performed to derive the dispersion relation and the stability condition. To this end, plane wave solutions of the form

$$\psi(\boldsymbol{r},t) = \begin{pmatrix} \mathscr{A}(\boldsymbol{p},E) \\ \mathscr{B}(\boldsymbol{p},E) \\ \mathscr{C}(\boldsymbol{p},E) \\ \mathscr{D}(\boldsymbol{p},E) \end{pmatrix} e^{\imath(\boldsymbol{p}\cdot\boldsymbol{r}-Et)},$$

with constant momentum $\boldsymbol{p}$ and energy E, are discretised on the stencil and inserted into the update equations (7). This results in a 4×4 matrix system with unknowns $\mathscr{A}$, $\mathscr{B}$, $\mathscr{C}$, and $\mathscr{D}$:

$$\begin{pmatrix} \mathscr{T}\mathscr{s} - (\mathscr{M}+\mathscr{V})\mathscr{c} & 0 & -\mathscr{P}_z & -\mathscr{P}_x + \imath\mathscr{P}_y \\ 0 & \mathscr{T}\mathscr{s} - (\mathscr{M}+\mathscr{V})\mathscr{c} & -\mathscr{P}_x - \imath\mathscr{P}_y & \mathscr{P}_z \\ -\mathscr{P}_z & -\mathscr{P}_x + \imath\mathscr{P}_y & \mathscr{T}\mathscr{s} - (-\mathscr{M}+\mathscr{V})\mathscr{c} & 0 \\ -\mathscr{P}_x - \imath\mathscr{P}_y & \mathscr{P}_z & 0 & \mathscr{T}\mathscr{s} - (-\mathscr{M}+\mathscr{V})\mathscr{c} \end{pmatrix} \begin{pmatrix} \mathscr{A}(\boldsymbol{p},E) \\ \mathscr{B}(\boldsymbol{p},E) \\ \mathscr{C}(\boldsymbol{p},E) \\ \mathscr{D}(\boldsymbol{p},E) \end{pmatrix} = 0,$$

in which we employed the shorthand notation

$$\mathscr{s} = \sin\left(\frac{E\Delta_t}{2}\right), \qquad \mathscr{c} = \cos\left(\frac{E\Delta_t}{2}\right),$$
$$\mathscr{T} = \frac{2}{\Delta_t}, \qquad \mathscr{V} = q\phi + V, \qquad \mathscr{M} = mc^2,$$
$$\mathscr{P}_l = c\frac{2}{\Delta_l}\sin\left(\frac{p_l\Delta_l}{2}\right) - qca_l\cos\left(\frac{p_l\Delta_l}{2}\right), \quad l = x,y,z.$$

This linear system only yields solutions if the matrix determinant is equal to zero. Enforcing this leads—after some simplifications—to the discrete dispersion relation of the minimally coupled Dirac equation:

$$\left[\frac{2}{\Delta_t}\sin\left(\frac{E\Delta_t}{2}\right) - (q\phi+V)\cos\left(\frac{E\Delta_t}{2}\right)\right]^2 = c^2\sum_{l=x,y,z}\left[\frac{2}{\Delta_l}\sin\left(\frac{p_l\Delta_l}{2}\right) - qa_l\cos\left(\frac{p_l\Delta_l}{2}\right)\right]^2 + \left(mc^2\right)^2\cos^2\left(\frac{E\Delta_t}{2}\right), \quad (8)$$

where we assumed for simplicity that $\boldsymbol{a}$, ϕ and V are constant in space and time. It is easily checked that in the continuum limit, i.e., $\Delta_\mu \to 0$, this equation converges to the dispersion relation of a relativistic particle in an electromagnetic field:

$$E^{\pm} = (q\phi + V) \pm \sqrt{\left(mc^2\right)^2 + (\boldsymbol{p} - q\boldsymbol{a})^2c^2}.$$

Combining the terms containing E in (8) into a single sine function and rearranging, gives

$$\sin^2(\mathscr{E}) = \frac{2\mathscr{P}^2 + \sqrt{\left(\mathscr{T}^2+\mathscr{V}^2-\mathscr{M}^2\right)^2 + 4\mathscr{T}^2\mathscr{M}^2} - \left(\mathscr{T}^2+\mathscr{V}^2-\mathscr{M}^2\right)}{2\sqrt{\left(\mathscr{T}^2+\mathscr{V}^2-\mathscr{M}^2\right)^2 + 4\mathscr{T}^2\mathscr{M}^2}}. \quad (9)$$

with

$$\mathscr{E} = \frac{E\Delta_t}{2} - \frac{1}{2}\arctan2\left(2\mathscr{T}\mathscr{V}, \mathscr{T}^2 - \mathscr{V}^2 + \mathscr{M}^2\right),$$
$$\mathscr{P}^2 = \mathscr{P}_x^2 + \mathscr{P}_y^2 + \mathscr{P}_z^2.$$

Since the energy E, and thus also $\mathscr{E}$, is a real number, the right hand side of (9) should be between 0 and 1, yielding

$$\mathscr{T}^2 \geq \frac{\mathscr{P}^2\left(\mathscr{P}^2 + \mathscr{M}^2 - \mathscr{V}^2\right)}{\mathscr{P}^2 + \mathscr{M}^2}.$$

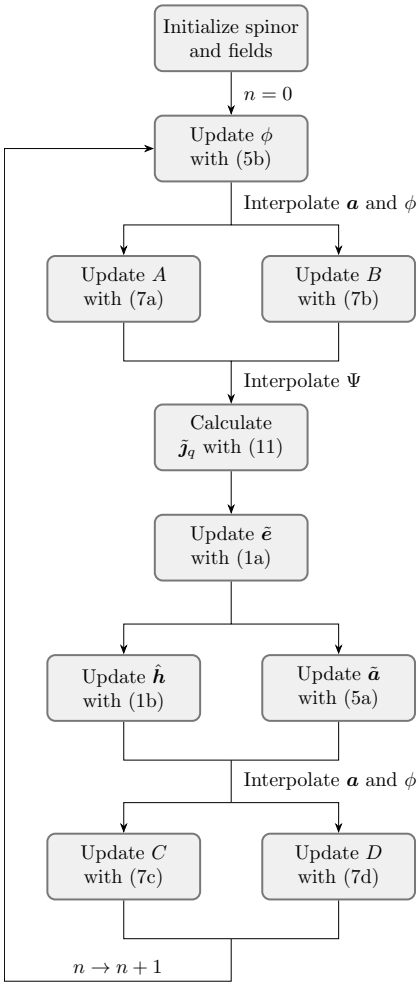

Figure 2: The proposed numerical scheme for the fully coupled Maxwell-Dirac system. The line splits where the order of the updates does not matter. As such, these updates can be easily parallelised.

This translates into the restriction on the time step given by

$$\Delta_t \leq 2 \sqrt{\frac{c^2 \sum_{l=1}^{3} \left(\frac{4}{\Delta_l^2} + q^2 a_l^2 \right) + (mc^2)^2}{c^2 \sum_{l=1}^{3} \left(\frac{4}{\Delta_l^2} + q^2 a_l^2 \right) \left[c^2 \sum_{l=1}^{3} \left(\frac{4}{\Delta_l^2} + q^2 a_l^2 \right) + (mc^2)^2 - (q\phi + V)^2 \right]}}, \tag{10}$$

where the maximum value of $\mathcal{P}^2$ was inserted to guarantee stability. When the potentials vanish, it is readily verified that the stability condition (10) for the advocated minimally coupled Dirac scheme coincides with the condition found in [16], which is exactly the CFL condition (2).

2.3. Fully coupled Maxwell-Dirac system

The forward coupling from Maxwell to Dirac was discussed in the previous section. For the backward coupling, the quantum current density $\boldsymbol{j}_q$ is defined as

$$\boldsymbol{j}_q = qc\psi^\dagger \boldsymbol{\alpha} \psi. \tag{11}$$

The spinor components are then interpolated in space and time to determine its discrete counterpart: the fore-vector $\tilde{\boldsymbol{j}}_q|^n_{\boldsymbol{m}}$. This quantity is introduced as an electromagnetic current source in (1a). A self-consistent FDTD scheme of the fully coupled system is now formed by combining (1), (5), (7), and (11). This novel method is schematically depicted in Fig. 2. Note again that the incorporation of (5b) into the scheme ensures that the Lorenz gauge is exactly satisfied on the discrete level, and that an overall second-order accuracy is obtained.

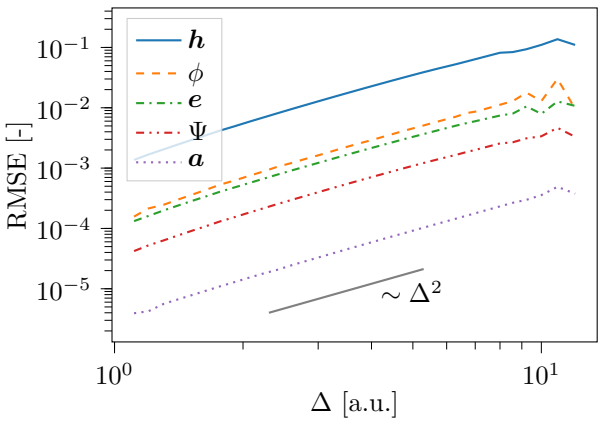

Figure 3: The root-mean-square error (RMSE) of all pertinent quantities exhibits second-order convergence as a function of the space-time grid step Δ.

Due to the non-linear nature of the coupling, a similar stability analysis of the Maxwell-Dirac scheme becomes intractable. However, through numerous simulation runs it was established that if both stability conditions, (2) and (10), are satisfied, the solution remains bounded. This conclusion is further corroborated by the simulations performed in the next sections.

3. Numerical validation of the method

We now discuss numerical results that validate the advocated method and demonstrate its merits. In the following simulations, the overall time step is chosen no higher than the minimum of (2) and (10).

3.1. Second-order accuracy

In all aforementioned update equations, the operators are approximated solely by second-order accurate differences and averages. Since both backward and forward coupling preserve this property, the novel fully coupled scheme is second-order accurate in space and time. This property is demonstrated by performing a range of simulations while varying the space and time steps. First, a reference simulation that consists of a free particle with mass $m = 0.023$ and charge $q = -1$ on a uniform space-time grid with dimensions $120\times120\times120$, in atomic units, and spatial step sizes $\Delta_x = \Delta_y = \Delta_z = \Delta = 0.6$ is run. The time step is determined from (2) for a CN of 0.2. The first spinor component is initialised as

$$A(x, y, z, 0) = \exp\left(-\frac{x^2 + y^2 + z^2}{4\sigma^2}\right),$$

with $\sigma = 6.594$. To ensure that the simulation is correctly initialised at $t = 0$, the first update of the quantities defined on half-integer time steps is modified to a first-order upwind step. This is achieved by simply replacing the central time differences by forward differences from $n = 0$ to $n = 1/2$, yielding a so-called "locally" second-order accurate scheme [33]. All other unknowns, as well as the external potential V, are initially set to zero. The simulation domain is terminated with homogeneous Dirichlet boundary conditions. After a simulation time of $t_{\max} = 3.03$, the program is halted. Next, this procedure is repeated for higher values of Δ, while keeping CN and $t_{\max}$ constant. For every simulation the root-mean-square error (RMSE) with respect to the reference simulation is calculated using

$$\mathrm{RMSE}_{\psi}^{n^*} = \sqrt{\frac{\sum\limits_{\text{grid points}} \left[\left(A^{n^*} - A_{\text{ref}}^{n^*}\right)^2 + \left(B^{n^*} - B_{\text{ref}}^{n^*}\right)^2 + \left(C^{n^*} - C_{\text{ref}}^{n^*}\right)^2 + \left(D^{n^*} - D_{\text{ref}}^{n^*}\right)^2\right]}{(N_x + 1)(N_y + 1)(N_z + 1)}},$$

in which n^* is the final time index. The reference solution is interpolated to match the grid points of the current simulation and the A and B components are interpolated in time. Analogous RMSE expressions are employed for the electric field, the magnetic field, and the EM potentials. The resulting relations between the RMSEs and the grid step size Δ are displayed in Fig. 3. It is observed that the presented scheme for the Maxwell-Dirac equations is indeed second-order accurate in both space and time, regardless of the first upwind step.

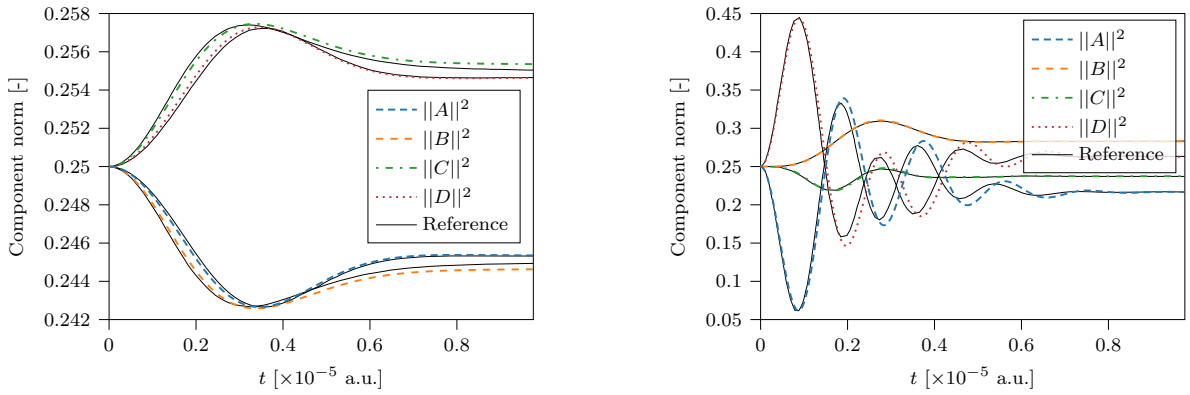

(a) Case 1

(b) Case 2

Figure 4: Norms of the four spinor components as a function of time for two cases (see Table 1). The results from [18] are displayed as solid black lines.

3.2. Comparison to an existing Maxwell-Dirac solver

To demonstrate the validity of our method, we replicate the results of a Maxwell-Dirac solver found in literature [18], where the influence of an initial EM field on a charged particle is investigated. The system describes an electron, i.e., $m = 1$ and $q = -1$, in a cubic simulation domain with a side length of 0.0107, which is divided into 128 cells in each direction, and CN = 0.0277 in the absence of an external potential ($V = 0$). The initial Dirac spinor is given by

$$\psi(\boldsymbol{r}, 0) = \psi_0 e^{-\frac{1}{2}\left(\gamma_1 x^2 + \gamma_2 y^2 + \gamma_3 z^2\right)} \begin{pmatrix} e^{\imath c_1 x} \\ e^{\imath c_2 x} \\ e^{\imath c_3 x} \\ e^{\imath c_4 x} \end{pmatrix}, \tag{12}$$

in which $\psi_0 = 3.47 \times 10^4$. The remaining parameter values are displayed in Table 1 for two cases. The initial time derivative of the magnetic potential in atomic units reads

$$\frac{\partial \boldsymbol{a}}{\partial t}(\boldsymbol{r}, 0) = -E_0 e^{-\kappa\left(x^2+y^2+z^2\right)}(\boldsymbol{u}_x + \boldsymbol{u}_y + \boldsymbol{u}_z),$$

with $E_0 = -2.81 \times 10^7$ and $\kappa = 8.95 \times 10^6$. This is translated into an initial condition for the electric field by recalling its relation to the EM potentials (3a), which results in

$$\begin{aligned} \boldsymbol{e}(\boldsymbol{r}, 0) &= -\boldsymbol{\nabla}\phi(\boldsymbol{r}, 0) - \frac{\partial \boldsymbol{a}}{\partial t}(\boldsymbol{r}, 0) \\ &= E_0 e^{-\kappa\left(x^2+y^2+z^2\right)}(\boldsymbol{u}_x + \boldsymbol{u}_y + \boldsymbol{u}_z), \end{aligned}$$

since the electric potential is initially equal to zero. Additionally, the magnetic vector potential and the magnetic field at $t = 0$ are set to zero. These initial conditions are then evaluated on the corresponding grid points and inserted into the coupled scheme. During each iteration the A- and B-components are interpolated in time, after which the norms of the four spinor components are calculated. Fig. 4 displays the norms of these four components for both cases, as well as the reference curves from [18]. A relative error of less than 0.1 % is measured for case 1 and less than 1 % for case 2. The slight deviations are caused by three main factors. First, method [18] solves the

Table 1: Parameter values adopted for the initial Dirac spinor in (12).

	γ_1	γ_2	γ_3	c_1	c_2	c_3	c_4
Case 1	4.47×10^6	6.71×10^6	8.95×10^6	-1.50×10^3	-1.50×10^3	-1.50×10^3	-1.50×10^3
Case 2	4.47×10^6	8.95×10^6	17.9×10^6	12.0×10^3	5.98×10^3	-5.98×10^3	1.50×10^3

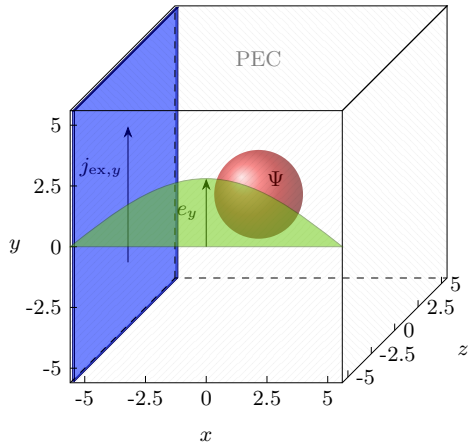

Figure 5: Schematic representation of a Dirac particle in an EM cavity, which is terminated by PECs. The current source sheet, shown in blue, excites the TE_{101} mode of the cavity. The corresponding profile of the electric field is depicted in green.

Dirac equation coupled to the wave equations for the EM potentials without taking the Lorenz gauge into account, while the advocated scheme solves the EM field equations alongside the gauge condition. Second, the scheme in [18] discretises the pertinent equations by combining spectral decomposition and the time-splitting procedure. The former method consists of expanding the spatial part of the unknowns into a Fourier series and solving the phase space equations, while the latter splits the time evolution operator into three parts in a second-order accurate way. This method is thus very different from our real-space FDTD approach. Third, the discretisation scheme from [16] defines the unknowns on a staggered grid, contrary to the collocated technique in [18]. The spurious solutions of the resulting discrete dispersion relation therefore introduce additional errors in their method.

4. Application examples

In this section, two practical examples of Maxwell-Dirac systems are presented. The first one deals with the modelling of a Dirac particle coupled to an EM cavity, showcasing the advocated scheme's conservation properties. In the second example, a waveguide consisting of the 3D Dirac material ZeTr_5 is simulated. It is shown that the charge carriers in this waveguide can indeed reach the Fermi velocity under the influence of EM fields, as such demonstrating the appositeness of the proposed method.

4.1. Simulation of a Dirac particle in an InAs quantum dot coupled to an EM cavity

In a closed system the Maxwell-Dirac equations have inherent symmetries, each leading to a conservation law as stated by Noether's theorem [34]. The most prominent examples are conservation of probability and conservation of energy. Consequently, an accurate scheme should be able to produce constant values for these quantities as a function of time, for closed systems. In this section, we present a modelling example which demonstrates that our method is capable of simulating this physical behaviour.

Similar to the approach in [35], we model an electron in an InAs quantum dot as a Dirac particle with $m = 0.023$ and $q = -1$ in the ground state of a harmonic oscillator (HO) electrostatic potential,

$$V(\boldsymbol{r}) = \frac{1}{2} m \omega_{\mathrm{HO}}^2 \boldsymbol{r}^2,$$

where $\omega_{\mathrm{HO}} = 57$, and with its spin oriented along the positive z-axis. This state was calculated via the solution method introduced in [36] by exploiting the rotational symmetry of the applied potential. Furthermore, the ground state energy of the Dirac particle was found to be $E_{\mathrm{D},0} = 521.065$. This particle is then placed inside a cubic EM cavity with dimensions $L_x = L_y = L_z = 11.202$, divided into 150 cells in each direction, which is surrounded by perfect electric conductors (PECs). This material is modelled by enforcing the tangential electric field, as well as the normal magnetic field, to vanish on the simulation boundary. The EM fields and potentials are initially set to zero and the cavity is then excited by an external current source sheet placed at a small distance from the boundary, as depicted in Fig. 5. It has a Gaussian-modulated sinusoidal time profile, defined as

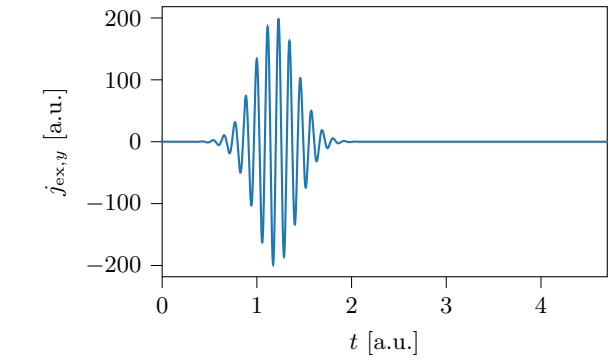

(a)

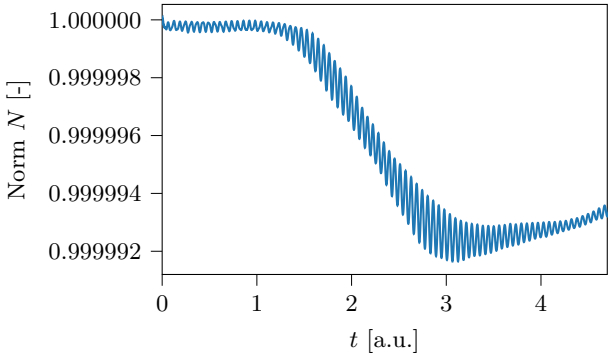

(b)

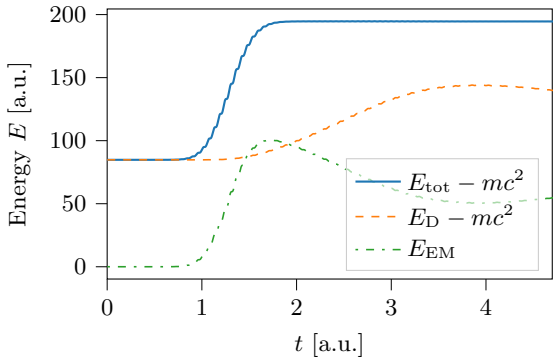

(c)

Figure 6: (a) The source profile, (b) the norm, and (c) the energy of a Dirac particle coupled to an EM cavity as a function of time. Both the norm and the total energy are conserved before and after the source has supplied energy to the system.

$$\boldsymbol{j}_{\mathrm{ex}}(t) = j_{y,0} \sin[\omega_{\mathrm{EM}}(t - t_0)] \exp\left[-\left(\frac{t - t_0}{t_w}\right)^2\right] \boldsymbol{u}_y,$$

with $j_{y,0} = 200$, $t_0 = 1.2$, and $t_w = 0.31831$, as illustrated in Fig. 6(a). The EM oscillation frequency ω_{EM} is tuned to the excitation energy of the Dirac particle, i.e.,

$$\omega_{\mathrm{EM}} = \Delta E_{\mathrm{D,ex}} = E_{\mathrm{D},1} - E_{\mathrm{D},0} = 54.351, \tag{13}$$

where the first excitation energy $E_{\mathrm{D},1} = 575.416$ was also determined by employing the strategy in [36]. Note that the value in (13) slightly differs from ω_{HO}, which is the excitation energy of a Schrödinger particle in a HO, due to the relativistic treatment of the system. The dimensions of the cavity are chosen such that the source also

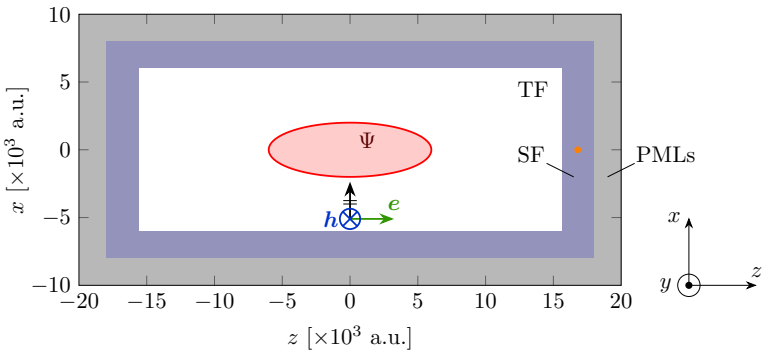

Figure 7: Schematic representation of the $ZrTe_5$ waveguide. The electron is graphically indicated in red and the electromagnetic fields $\boldsymbol{e}$ and $\boldsymbol{h}$, originating from the total-field (TF) scattered-field (SF) boundary, are coloured green and blue, respectively. The domain is terminated with perfectly matched layers (PMLs). The orange dot indicates the location in the SF region where the electric field is recorded.

excites the first transversal electric eigenmode in the y-direction (TE_{101}), with its eigenfrequency given by [37]

$$\omega_{\mathrm{TE}_{101}} = c\sqrt{\left(\frac{\pi}{L_x}\right)^2 + \left(\frac{\pi}{L_z}\right)^2} = 54.351.$$

The profile of the electric field corresponding to this mode is displayed in green in Fig. 5. With this careful construction of the setup, the EM cavity is strongly coupled to the Dirac particle and energy transfer between the EM and QM parts is maximised.

To show the conservation of probability, the total norm N, given by

$$N = \int_{V_{\mathrm{sim}}} \psi^\dagger \psi \, \mathrm{d}\boldsymbol{r},$$

where V_{sim} represents the simulation space, is calculated by means of numerical integration using the trapezoidal rule [38]. To this end, the spinor components are interpolated in space and time so that they are defined on the same space-time points. Likewise, the numerical energies of the Dirac particle and the EM field are found by discretising their respective analytical expressions [32, 37]:

$$E_{\mathrm{D}} = \int_{V_{\mathrm{sim}}} \psi^\dagger \left(\imath \frac{\partial}{\partial t} - q\phi\right)\psi \, \mathrm{d}\boldsymbol{r},$$
$$E_{\mathrm{EM}} = \int_{V_{\mathrm{sim}}} \frac{1}{2}\left(\epsilon_0 \boldsymbol{e}^2 + \mu_0 \boldsymbol{h}^2\right) \mathrm{d}\boldsymbol{r}.$$

Due to time translation symmetry in the absence of sources, the total energy of the system,

$$E_{\mathrm{tot}} = E_{\mathrm{D}} + E_{\mathrm{EM}},$$

should then be conserved.

The Courant number is set to 0.1 and the simulation is run for 150 000 iterations, yielding the results displayed in Fig. 6. Fig. 6(b) shows the total norm as a function of time. A deviation on the order of 10^{-6} is observed, meaning that it is indeed conserved. The energies of the Dirac particle and the EM field, as well as the total energy, are presented in Fig. 6(c). As can be seen, during the first iterations the total energy is conserved since no currents are present. When the source is active, the EM field rapidly gains energy and, after the current has petered out, energy is still transferred between the EM field and the Dirac particle at a slower pace, while the total energy again remains constant. Relative fluctuations on the order of 10^{-4} are observed.

These results demonstrate that even when a considerable amount of energy is exchanged, our proposed method conserves the total norm and energy with deviations of at most 0.01 %.

4.2. Modelling of charge carriers in a $ZrTe_5$ waveguide

The 3D Dirac material $ZrTe_5$ is modelled around the Γ-point, where a linear dispersion relation was measured with a small mass gap [39] such that the charge carriers inside this transition metal are governed by an anisotropic

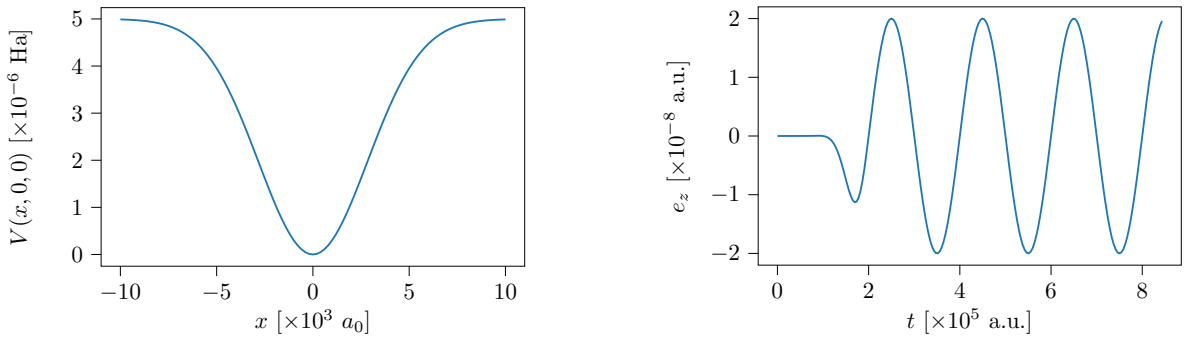

(a) (b)

Figure 8: (a) The potential profile of the $ZrTe_5$ waveguide in the x-direction and (b) the waveform of the EM source as a function of time.

Dirac Hamiltonian [40]. Consequently, the Dirac equation (6) requires some modification, as detailed in Appendix B. The speed of light is replaced by the anisotropic Fermi velocity ν_l in each spatial direction, $l = x, y, z$. and the rest energy becomes half of the band gap $E_g/2$. Furthermore, the dielectric constant of $ZrTe_5$ is set to 25.3 [40], meaning that ϵ_0 and $c = 1/\sqrt{\mu_0\epsilon_0}$ are scaled accordingly.

We now take advantage of the elevated carrier mobility in $ZrTe_5$ by constructing a 3D waveguide, intended to serve as a new type of conductive channel in a transistor. Since the Fermi velocity in the z-direction is much higher ($\approx 3.49 \times 10^5$ m/s in SI units) than along the transversal directions, the material is aligned along this z-axis. As displayed in Fig. 7, an electron inside a waveguide with dimensions $20\,000 \times 8000 \times 40\,000$, in atomic units, is modelled. It is contained in the x- and y-directions by an electrostatic potential, given by

$$V(x, y, z) = V_0 \left[1 - \exp\left(-\frac{x^2 + y^2}{r_0^2}\right)\right],$$

with $V_0 = 5 \times 10^{-6}$ and $r_0 = 4000$, while being free to move in the z-direction. The potential profile is shown in Fig. 8(a). The ground state of the first transversal mode was again calculated as in [36], and the electron is represented as a free wave packet along the z-axis, with its spin oriented towards the positive z-direction. The waveguide is excited by a z-polarised EM plane wave propagating in the x-direction. The linear polarisation of the electric field causes the particle to accelerate along its free axis. The waveform of the corresponding e_z-component is a ramped-up sine wave, defined as

$$e_z(t) = \begin{cases} E_0 \sin(\omega t) \exp\left\{-\left[4\omega(t - \frac{2\pi}{\omega})\right]^2\right\}, & t < \frac{2\pi}{\omega}, \\ E_0 \sin(\omega t), & t \geq \frac{2\pi}{\omega}, \end{cases}$$

with $E_0 = 2 \times 10^{-8}$ and $\omega = 3.14 \times 10^{-5}$, and is depicted in Fig. 8(b). The plane wave is implemented as a total-field scattered-field (TFSF) source [23] and the simulation domain of the EM part is terminated with perfectly matched layers (PMLs) to avoid reflections from the boundaries. Dirichlet boundary conditions are used for the Dirac part.

Owing to the introduction of the Fermi velocities in the Dirac equation, the stability condition (2) of the FDTD method now constitutes the strictest limit on the time step and we choose CN = 1. A total time of 848 000, or 20.5 ps, is simulated, while recording the average position of the electron as well as the electric field at $(0, 0, 16\,800)$, i.e., inside the scattered field (SF) region. These quantities are plotted in Fig. 9. The inertia of the particle leads to a delay of about 100 000 time units until it start moving, as seen in Fig. 9(a). Our model correctly predicts that the motion is opposite to that of the electric field, since the electron is negatively charged. Figure 9(b) shows that the charged particle creates its own EM field once it starts moving. This field is about 10 times smaller than the applied field and is predominantly polarised along the z-axis, which can be explained by making an analogy between the oscillating charged particle and a Hertzian dipole's near-field characteristics. By calculating the time derivative of the average position, the velocity is found to reach 80 % of the Fermi velocity ν_z. This is remarkable because the maximum electric field strength (≈ 0.01 kV/nm) is small compared to typical values in modern nanoelectronics [41]. It can thus be concluded that the charge carriers in $ZrTe_5$ are indeed easily accelerated to the Fermi velocity, corroborating the importance of Dirac materials for inclusion in novel nanodevices.

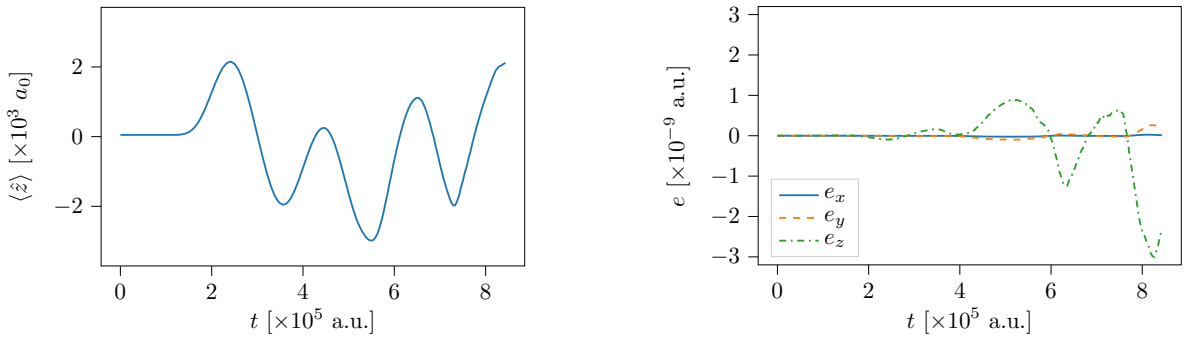

(a) (b)

Figure 9: (a) Average z-position of the electron in the $ZrTe_5$ waveguide and (b) generated electric field at $(0, 0, 16\,800)$ as a function of time.

To finish this section, the CPU time of the simulations from Section 3 and those from this section are listed in Table 2. The calculations were performed on 48 Intel(R) Xeon(R) Gold 6136 CPU processors with a base clock rate of 3.00 GHz. The code was implemented in the C programming language and parallelised with the OpenMP API to fully optimise the run times.

Table 2: CPU times of the simulations performed in this paper.

Simulation	Section	CPU time [s]
Accuracy (Reference)	3.1	1263
Comparison	3.2	723
Cavity	4.1	190 927
Waveguide	4.2	18 828

5. Conclusion

A novel method to solve the fully coupled Maxwell-Dirac equations is devised, targeting the accurate, multi-physics modelling of Dirac materials for integration into nanoelectronic devices. It combines the well-known FDTD method for Maxwell's equations and a real-space time-domain scheme for the Dirac equation through, on the one hand, minimal coupling and, on the other hand, introduction of the quantum current density in Ampère's law. To this end, a new discretisation of both the minimally-coupled Dirac equation and the quantum current density is performed, and the stability condition of the former is derived. The resulting expression properly coincides with the Courant-Friedrichs-Lewy condition when the EM fields are zero.

The scheme is carefully constructed, such that the second-order accuracy of the individual methods is preserved. Plotting the error with respect to a reference simulation showed a quadratic convergence rate, confirming the second-order accuracy of our solver. Two numerical examples from literature are then replicated and errors on the order of only 0.1 % and 1 % are found, which validates the novel scheme.

Next, we consider a closed system consisting of a Dirac particle in an EM cavity, which enables the analysis of conservation of norm and energy. We find that our method conserves these quantities with maximal deviations on the order of 0.01 %. Furthermore, the Lorenz gauge is exactly satisfied on a discrete level, in contrast to the solvers presented in previous works where the gauge is dependent on the initial conditions. This inevitably leads to unphysical results and renders the simulation of Dirac devices impossible.

Moreover, the proposed solver solves for the electric and magnetic fields, instead of solely the potentials, allowing for a seamless integration into existing EM-FDTD frameworks and, conversely, facilitating the implementation of methods known from CEM into our code. We show this by means of a final practical application example of a $ZrTe_5$ waveguide. The TFSF technique is implemented to simulate EM plane waves impinging on particles in this waveguide, and the domain is terminated with PMLs. Since TFSF and PMLs are well-established concepts from CEM and the proposed scheme directly utilises the FDTD technique, no extra derivations were needed. In contrast, as 3D Dirac materials, like $ZrTe_5$, often exhibit anisotropic properties, the modelling becomes more

intricate but it is shown that this can be handled by our versatile approach. The results show that the electrons in this waveguide are easily accelerated to high velocities, i.e., around 80 % of the Fermi velocity, or 2.79×10^5 m/s. Therefore, 3D Dirac materials are attracting more and more attention as alternatives or extensions to conventional semiconductor-based devices.

Further research can now be conducted to extend the modelling possibilities for these emerging Dirac devices. For example, it is possible to include dielectric materials, like SiO_2, which are prevalent in nanoelectronics. Also, to further improve the modelling of real-life devices, contacts can be investigated and implemented as potential barriers, for instance. Furthermore, to increase the simulation dimensions to that of full-sized devices, higher-order schemes can be implemented by replacing the discrete operators introduced in Section 2.2.1 by higher-order finite differences. As such, the need for dense grids is alleviated, which will result in the multiphysics characterisation of full Dirac nanodevices, envisioning diodes, transistors, spintronic and valleytronic devices, etc. These research paths are open for further exploration.

Acknowledgements

The authors would like to thank Research Foundation - Flanders (FWO) for supporting this research (1101722N).

Appendix A. Discrete calculus notation

In this appendix, an overview of the definitions introduced in [30] is given. The following expressions all tend to their analytical equivalent as $\Delta_\mu \to 0$, $\mu = t, x, y, z$.

Discrete derivative

The forward discrete derivative is denoted with a tilde and is defined as

$$\tilde{\partial}_x f_i = \frac{f_{i+1} - f_i}{\Delta_x}.$$

The resulting expression is will be evaluated at $x = (i + 1/2)\Delta_x$. The backward equivalent is labelled with a hat, as follows

$$\hat{\partial}_x f_i = \frac{f_i - f_{i-1}}{\Delta_x},$$

and is used at on $x = (i - 1/2)\Delta_x$. Since both these discrete derivatives only appear in a context where they are evaluated at $x = (i \pm 1/2)\Delta_x$, they are of order $\mathcal{O}(\Delta_x^2)$. The discrete derivatives in the y-, z- and t-dimensions are completely analogous.

Discrete vector fields

Two types of discrete vector fields are presented. The first type consists of fore-vectors at discrete points (i, j, k) and is written as

$$\tilde{\boldsymbol{F}}^n_{i,j,k} = F_x|^n_{i+\frac{1}{2},j,k}\boldsymbol{u}_x + F_y|^n_{i,j+\frac{1}{2},k}\boldsymbol{u}_y + F_z|^n_{i,j,k+\frac{1}{2}}\boldsymbol{u}_z,$$

with unit vectors $\boldsymbol{u}_l$, $l = x, y, z$, in the three spatial dimensions. Here, the time index n is also displayed to ensure that the notation is consistent with the main content of this paper. The second type of vector field is described by back-vectors, i.e.,

$$\hat{\boldsymbol{F}}^n_{i,j,k} = F_x|^n_{i-\frac{1}{2},j,k}\boldsymbol{u}_x + F_y|^n_{i,j-\frac{1}{2},k}\boldsymbol{u}_y + F_z|^n_{i,j,k-\frac{1}{2}}\boldsymbol{u}_z.$$

Similar to the discrete derivatives, a tilde represents a forward movement in space, while a hat signifies a backward step. To improve readability, a vertical line is inserted before the indices of discrete vector components.

Discrete gradient

The discrete counterparts of the gradient are expressed as

$$\tilde{\nabla} f^n_{i,j,k} = \tilde{\partial}_x f^n_{i,j,k}\boldsymbol{u}_x + \tilde{\partial}_y f^n_{i,j,k}\boldsymbol{u}_y + \tilde{\partial}_z f^n_{i,j,k}\boldsymbol{u}_z$$
$$\hat{\nabla} f^n_{i,j,k} = \hat{\partial}_x f^n_{i,j,k}\boldsymbol{u}_x + \hat{\partial}_y f^n_{i,j,k}\boldsymbol{u}_y + \hat{\partial}_z f^n_{i,j,k}\boldsymbol{u}_z$$

for a discretised scalar function f. The result of the forward gradient is a fore-vector and that of the backward variant a back-vector.

Discrete divergence

The discrete divergence of a fore-vector field is defined as follows

$$\hat{\nabla}\cdot\tilde{\boldsymbol{F}}^n_{i,j,k}=\hat{\partial}_x F_x|^n_{i+\frac{1}{2},j,k}+\hat{\partial}_y F_y|^n_{i,j+\frac{1}{2},k}+\hat{\partial}_z F_z|^n_{i,j,k+\frac{1}{2}},$$

while the divergence of a back-vector field is given by

$$\tilde{\nabla}\cdot\hat{\boldsymbol{F}}^n_{i,j,k}=\tilde{\partial}_x F_x|^n_{i-\frac{1}{2},j,k}+\tilde{\partial}_y F_y|^n_{i,j-\frac{1}{2},k}+\tilde{\partial}_z F_z|^n_{i,j,k-\frac{1}{2}}.$$

The alternation between tildes and hats leads to an accuracy of $\mathcal{O}(\Delta_l^2)$, $l=x,y,z$, at the point (i,j,k).

Discrete curl

The forward curl is approximated as

$$\begin{aligned}\tilde{\nabla}\times\tilde{\boldsymbol{F}}^n_{i,j,k}=&\left[\tilde{\partial}_y F_z|^n_{i,j,k+\frac{1}{2}}-\tilde{\partial}_z F_y|^n_{i,j+\frac{1}{2},k}\right]\boldsymbol{u}_x\\&+\left[\tilde{\partial}_z F_x|^n_{i+\frac{1}{2},j,k}-\tilde{\partial}_x F_z|^n_{i,j,k+\frac{1}{2}}\right]\boldsymbol{u}_y\\&+\left[\tilde{\partial}_x F_y|^n_{i,j+\frac{1}{2},k}-\tilde{\partial}_y F_x|^n_{i+\frac{1}{2},j,k}\right]\boldsymbol{u}_z,\end{aligned}$$

which results in a back-vector associated with the point $(i+1/2,j+1/2,k+1/2)$. Equivalently, the backward curl is given by

$$\begin{aligned}\hat{\nabla}\times\hat{\boldsymbol{F}}^n_{i,j,k}=&\left[\hat{\partial}_y F_z|^n_{i,j,k-\frac{1}{2}}-\hat{\partial}_z F_y|^n_{i,j-\frac{1}{2},k}\right]\boldsymbol{u}_x\\&+\left[\hat{\partial}_z F_x|^n_{i-\frac{1}{2},j,k}-\hat{\partial}_x F_z|^n_{i,j,k-\frac{1}{2}}\right]\boldsymbol{u}_y\\&+\left[\hat{\partial}_x F_y|^n_{i,j-\frac{1}{2},k}-\hat{\partial}_y F_x|^n_{i-\frac{1}{2},j,k}\right]\boldsymbol{u}_z\end{aligned}$$

and translates to a fore-vector defined on $(i-1/2,j-1/2,$
$k-1/2)$. These expressions are also of order $\mathcal{O}(\Delta_l^2)$.

Appendix B. Anisotropic Dirac equation to model $ZrTe_5$

In [40], the Hamiltonian for $ZrTe_5$ around the Γ-point is modelled in momentum space as follows:

$$H_{\mathrm{ZrTe_5}}(\boldsymbol{p})=\frac{E_g}{2}(\sigma_z\otimes\mathbb{1}_2)+\nu_x p_x(\sigma_x\otimes\sigma_z)+\nu_y p_y(\sigma_x\otimes\sigma_x)+\nu_z p_z(\sigma_y\otimes\mathbb{1}_2),$$

with the energy gap denoted as $E_g=7.35\times10^{-4}$ and the Fermi velocities as $\nu_x=0.0532$, $\nu_y=0.00701$, and $\nu_z=0.159$, all given in atomic units. The main axes, a, b, and c, of the material are chosen to coincide with the spatial coordinate axes x, y, and z, respectively. To achieve this, the unitary transformation matrix

$$U=\frac{1}{\sqrt{2}}\begin{pmatrix}-1&\imath&0&0\\\imath&-1&0&0\\0&0&\imath&1\\0&0&-1&-\imath\end{pmatrix}$$

is applied to the Hamiltonian, yielding the anisotropic Dirac Hamiltonian

$$H_{\mathrm{model}}(\boldsymbol{p})=UH_{\mathrm{ZrTe_5}}(\boldsymbol{p})U^\dagger=\begin{pmatrix}E_g/2&0&\nu_z p_z&\nu_x p_x-\imath\nu_y p_y\\0&E_g/2&\nu_x p_x+\imath\nu_y p_y&-\nu_z p_z\\\nu_z p_z&\nu_x p_x-\imath\nu_y p_y&-E_g/2&0\\\nu_x p_x+\imath\nu_y p_y&-\nu_z p_z&0&-E_g/2\end{pmatrix}.$$

The coordinate representation of this Hamiltonian now matches the right-hand side of 6 without EM fields upon interchanging the rest energy by $E_g/2$, and the speed of light c with the Fermi velocity in the respective direction. The update equations (7) of the Dirac part are therefore adapted by making the following replacements:

$$\begin{aligned} mc^2 &\to E_g/2, \\ c\mathcal{D}_x &\to \nu_x(\partial_x - \imath q a_x \mathcal{M}_x), \\ c\mathcal{D}_y &\to \nu_y(\partial_y - \imath q a_y \mathcal{M}_y), \\ c\mathcal{D}_z &\to \nu_z(\partial_z - \imath q a_z \mathcal{M}_z). \end{aligned}$$

Finally, the expression of the quantum current density also requires a small adjustment, i.e.,

$$j_{q,l} = q\nu_l \psi^\dagger \alpha_l \psi, \qquad\qquad l = x, y, z,$$

which completes the transformation of the original scheme to the anisotropic Dirac Hamiltonian of $ZrTe_5$.

References

[1] J. Shalf, The future of computing beyond Moore's law, Philosophical Transactions of the Royal Society A 378 (2020). doi:10.1098/rsta.2019.0061, 20190061.

[2] T. O. Wehling, A. M. Black-Schaffer, A. V. Balatsky, Dirac materials, Advances in Physics 63 (2014) 1–76. doi:10.1080/00018732.2014.927109.

[3] P. V. Ratnikov, A. P. Silin, Two-dimensional graphene electronics: current status and prospects, Physics-Uspekhi 61 (2018) 1139–1174. doi:10.3367/ufne.2017.11.038231.

[4] F. Xiu, T. Zhao, Topological insulator nanostructures and devices, Chinese Physics B 22 (2013). doi:10.1088/1674-1056/22/9/096104, 096104.

[5] N. P. Armitage, E. J. Mele, A. Vishwanath, Weyl and Dirac semimetals in three-dimensional solids, Reviews of Modern Physics 90 (2018). doi:10.1103/RevModPhys.90.015001, 015001.

[6] J. R. Bayogan, K. Park, Z. B. Siu, S. J. An, C.-C. Tang, X.-X. Zhang, M. S. Song, J. Park, M. B. A. Jalil, N. Nagaosa, K. Hirakawa, C. Schoenenberger, J. Seo, M. Jung, Controllable p-n junctions in three-dimensional Dirac semimetal Cd3As2 nanowires, Nanotechnology 31 (2020). doi:10.1088/1361-6528/ab6dfe, 205001.

[7] Y.-F. Wu, L. Zhang, C.-Z. Li, Z.-S. Zhang, S. Liu, Z.-M. Liao, D. Yu, Dirac semimetal heterostructures: 3D Cd3As2 on 2D graphene, Advanced Materials 30 (2018). doi:10.1002/adma.201707547, 1707547.

[8] X. Zhang, R. Pan, Y. Yang, J. H. X. Liu, H. Zhou, J. Gou, F. Xiu, J. Wang, 3D Dirac semimetal Cd3As2/CuPc heterojunction for promoted visible-infrared photo-detection, Optical Materials 111 (2021). doi:10.1016/j.optmat.2020.110699, 110699.

[9] J. Chen, T. Zhang, J. Wang, N. Zhang, W. Ji, S. Zhou, Y. Chai, Field-effect chiral anomaly devices with Dirac semimetal, Advanced Functional Materials 31 (2021). doi:10.1002/adfm.202104192, 2104192.

[10] Z. Xie, X. Wei, S. Cao, Y. Zhang, S. Yan, G. D. Gu, Q. Li, J.-H. Chen, Electron-electron interactions and weak antilocalization in few-layer $Zrte_5$ devices, Physics Review B 103 (2021). doi:10.1103/PhysRevB.103.155408, 155408.

[11] J. Hu, S.-Y. Xu, N. Ni, Z. Mao, Transport of topological semimetals, in: Annual Review of Materials Research, volume 49, 2019, pp. 207–252. doi:10.1146/annurev-matsci-070218-010023.

[12] J. Wu, J. J. Bai, R. Y. Cusson, Numerical method for the time evolution of the Dirac equation, Zeitschrift für Physik A Hadrons and Nuclei 335 (1990) 125–130. doi:10.1007/BF01294466.

[13] J. W. Braun, Q. Su, R. Grobe, Numerical approach to solve the time-dependent Dirac equation, Physical Review A 59 (1999) 604–612. doi:10.1103/PhysRevA.59.604.

[14] F. Fillion-Gourdeau, E. Lorin, A. D. Bandrauk, Numerical solution of the time-dependent Dirac equation in coordinate space without fermion-doubling, Computer Physics Communications 183 (2012) 1403–1415. doi:10.1016/j.cpc.2012.02.012.

[15] M. Almquist, K. Mattsson, T. Edvinsson, High-fidelity numerical solution of the time-dependent Dirac equation, Journal of Computational Physics 262 (2014) 86–103. doi:10.1016/j.jcp.2013.12.038.

[16] R. Hammer, W. Pötz, A. Arnold, Single-cone real-space finite difference scheme for the time-dependent Dirac equation, Journal of Computational Physics 265 (2014) 50–70. doi:10.1016/j.jcp.2014.01.028.

[17] W. Bao, Y. Cai, X. Jia, Q. Tang, Numerical methods and comparison for the Dirac equation in the nonrelativistic limit regime, Journal of Scientific Computing 71 (2017) 1094–1134. doi:10.1007/s10915-016-0333-3.

[18] W. Bao, X. Li, An efficient and stable numerical method for the Maxwell-Dirac system, Journal of Computational Physics 199 (2004) 663–687. doi:10.1016/j.jcp.2004.03.003.

[19] Z. Huang, S. Jin, P. Markowich, C. Sparber, C. Zheng, A time-splitting spectral scheme for the Maxwell–Dirac system, Journal of Computational Physics 208 (2005) 761–789. doi:10.1016/j.jcp.2005.02.026.

[20] X. Li, C. K. Chan, Y. Hou, A numerical method with particle conservation for the Maxwell-Dirac system, Applied Mathematics and Computation 216 (2010) 1096–1108. doi:10.1016/j.amc.2010.02.002.

[21] E. Lorin, A. Bandrauk, A simple and accurate mixed P0-Q1 solver for the Maxwell-Dirac equations, Nonlinear Analysis: Real World Applications 12 (2011) 190–202. doi:10.1016/j.nonrwa.2010.06.007.

[22] Y. Fu, L. Cao, The Crank–Nicolson Galerkin method and convergence for the time-dependent Maxwell–Dirac system under the Lorentz gauge, Journal of Computational and Applied Mathematics 407 (2022). doi:10.1016/j.cam.2021.114007, 114007.

[23] A. Taflove, S. C. Hagness, Computational Electrodynamics: The Finite-Difference Time-Domain Method, third ed., Artech House, 2005.

[24] T. Namiki, A new FDTD algorithm based on alternating-direction implicit method, IEEE Transactions on Microwave Theory and Techniques 47 (1999) 2003–2007. doi:10.1109/22.795075.

[25] Y. Yang, R. S. Chen, E. K. N. Yung, The unconditionally stable Crank Nicolson FDTD method for three-dimensional Maxwell's equations, Microwave and Optical Technology Letters 48 (2006) 1619–1622. doi:10.1002/mop.21684.

[26] A. Van Londersele, D. De Zutter, D. Vande Ginste, An in-depth stability analysis of nonuniform FDTD combined with novel local implicitization techniques, Journal of Computational Physics 342 (2017) 177–193. doi:10.1016/j.jcp.2017.04.036.

[27] A. Wharmby, R. Bagley, Modifying Maxwell's equations for dielectric materials based on techniques from viscoelasticity and concepts from fractional calculus, International Journal of Engineering Science 79 (2014) 59–80. doi:10.1016/j.ijengsci.2014.02.004.

[28] J. Smit, Introduction to Quantum Fields on a Lattice, Cambridge Lecture Notes in Physics, Cambridge University Press, 2002. doi:10.1017/CBO9780511583971.

[29] I. Montvay, G. Münster, Quantum Fields on a Lattice, Cambridge Monographs on Mathematical Physics, Cambridge University Press, 1994. doi:10.1017/CBO9780511470783.

[30] W. C. Chew, Electromagnetic theory on a lattice, Journal of Applied Physics 75 (1994) 4843–4850. doi:10.1063/1.355770.

[31] L. E. F. F. Torres, S. Roche, J. Charlier, Introduction to Graphene-Based Nanomaterials: From Electronic Structure to Quantum Transport, 2 ed., Cambridge University Press, 2020. doi:10.1017/9781108664462.

[32] W. Greiner, Relativistic Quantum Mechanics. Wave Equations, third ed., Springer, 2000.

[33] O. Pinaud, Absorbing layers for the Dirac equation, Journal of Computational Physics 289 (2015) 169–180. doi:10.1016/j.jcp.2015.02.049.

[34] J. Read, N. J. Teh, The Philosophy and Physics of Noether's Theorems: A Centenary Volume, Cambridge University Press, 2022. doi:10.1017/9781108665445.

[35] C. J. Ryu, A. Y. Liu, W. E. I. Sha, W. C. Chew, Finite-difference time-domain simulation of the Maxwell–Schrödinger system, IEEE Journal on Multiscale and Multiphysics Computational Techniques 1 (2016) 40–47. doi:10.1109/JMMCT.2016.2605378.

[36] R. R. Silbar, T. Goldman, Solving the radial Dirac equations: a numerical odyssey, European Journal of Physics 32 (2010) 217–233. doi:10.1088/0143-0807/32/1/021.

[37] J. D. Jackson, Classical Electrodynamics, 3 ed., Wiley, 1999. doi:10.1119/1.19136.

[38] K. E. Atkinson, An Introduction to Numerical Analysis, second ed., Wiley, 2008.

[39] C. R. Y., S. J. Zhang, J. A. Schneeloch, C. Zhang, Q. Li, G. D. Gu, N. L. Wang, Optical spectroscopy study of the three-dimensional Dirac semimetal zrte$_5$, Physical Review B 92 (2015). doi:10.1103/PhysRevB.92.075107, 075107.

[40] S. Galeski, T. Ehmcke, R. Wawrzyńczak, P. M. Lozano, K. Cho, A. Sharma, S. Das, F. Küster, P. Sessi, M. Brando, R. Küchler, A. Markou, M. König, P. Swekis, C. Felser, Y. Sassa, Q. Li, G. Gu, M. V. Zimmermann, O. Ivashko, D. I. Gorbunov, S. Zherlitsyn, T. Förster, S. S. P. Parkin, J. Wosnitza, T. Meng, J. Gooth, Origin of the quasi-quantized Hall effect in $ZrTe_5$, Nature Communications 12 (2021). doi:10.1038/s41467-021-23435-y, 3197.

[41] K. Xu, M. M. Islam, D. Guzman, A. C. Seabaugh, A. Strachan, S. K. Fullerton-Shirey, Pulse dynamics of electric double layer formation on all-solid-state graphene field-effect transistors, ACS Applied Materials & Interfaces 10 (2018) 43166–43176. doi:10.1021/acsami.8b13649.